PAPER

Check for updates

S-doped C₃N₅ derived from thiadiazole for efficient photocatalytic hydrogen evolution†

Xinwei Guan, [ID] [a] Mohammed Fawaz,[a] Ranjini Sarkar,[b] Chun-Ho Lin, [ID] [c] Zhixuan Li,[a] Zhihao Lei,[a] Panangattu Dharmarajan Nithinraj,[a] Prashant Kumar, [ID] [a] Xiangwei Zhang,[a] Jae-Hun Yang,[a] Long Hu,[c] Tom Wu, [ID] [cd] Sudip Chakraborty,[b] Jiabao Yi*[a] and Ajayan Vinu [ID] *[a]

Graphitic carbon nitrides (g-C₃N₄) with unique physicochemical properties are promising candidates for photocatalysis applications. However, pristine g-C₃N₄ often suffers from narrow absorption ranges and high carrier recombination rates, which result in mediocre catalytic performance. In this work, we prepare novel sulfur-doped high nitrogen containing carbon nitrides, C₃N₅ (SCNs), with a combined thiadiazole, triazole, and triazine framework by facile self-assembly of 5-amino-1,3,4-thiadiazole-2-thiol (5-ATDT). Their structural, morphological, and optical properties, and photocatalytic activities are investigated in detail. From density functional theory calculations and spectroscopic characterization studies, we construct thermodynamically stable molecular structures of SCNs composed of one triazole and two triazine moieties with small ratios of thiadiazole on the edge, in which the sulfur atoms are ionically connected with carbon/nitrogen atoms and gradually detached on increasing the calcination temperatures. Remarkably, the resultant SCNs exhibit a significantly enhanced H₂-generation rate of 486 μmol g⁻¹ h⁻¹, about 60% higher than the average value derived from typical g-C₃N₄ synthesised by conventional precursors thanks to the enlarged light absorption range and enhanced charge carrier transfer rate. Our work provides a unique approach for designing novel sulfur-doped carbon nitrides with unprecedented functionalities.

10th anniversary statement

Journal of Materials Chemistry A celebrates its 10th anniversary. To our surprise, our group has consistently contributed to the *Journal of Materials Chemistry A* for the last 10 years. The journal has achieved its original mission of publishing quality reports from interdisciplinary communities and providing an efficient and rigorous service to scientists across diverse fields spanning across materials chemistry. Many of our previous studies published in the *Journal of Materials Chemistry A*, related to carbon/carbon nitrides in energy and environmental fields, have drawn profound attention, which in turn inspired enormous follow-up research endeavours. In addition, we have summarized several comprehensive reviews with a broader outlook and perspective on these topics and received a significant amount of citations. These achievements have helped our group to build a reputation and establish international collaborations, further deepening our understanding in these fields, which also helps us to expand the research fields, promote the research level, educate younger researchers, and convert the research results to industrial products. I sincerely believe that the valuable research published in this edition will make a long-lasting impact and will significantly contribute to human progress in energy and sustainability. This will be perhaps the best way to celebrate the 10th anniversary of *Journal of Materials Chemistry A*.

[a]Global Innovative Centre for Advanced Nanomaterials, School of Engineering, College of Engineering, Science and Environment, The University of Newcastle, Callaghan, NSW, 2308, Australia. E-mail: jiabao.yi@newcastle.edu.au; ajayan.vinu@newcastle.edu.au

[b]Materials Theory for Energy Scavenging (MATES) Lab, Harish-Chandra Research Institute (HRI) Allahabad, HBNI, Chhatnag Road, Jhunsi, Prayagraj (Allahabad), 211019, India

[c]School of Materials Science and Engineering, University of New South Wales (UNSW), Sydney, NSW, 2052, Australia

[d]Department of Applied Physics, The Hong Kong Polytechnic University, Hung Hom, Hong Kong, 999077, P. R. China

† Electronic supplementary information (ESI) available. See DOI: https://doi.org/10.1039/d3ta00318c

g-C₃N₄ with sp²-hybridized carbon and nitrogen has drawn prodigious attention owing to its unique physicochemical properties,[1–4] including low-cost, tunable bandgaps, excellent thermal conductivity, semiconductivity, and biocompatibility, enabling it to have a broad range of applications in adsorption,[5] photocatalysis,[6] electrocatalysis,[7] energy storage and conversion,[8] and sensing.[9] The performance of g-C₃N₄ in these applications is highly relevant to its porosity, crystal structure, crystallinity, and element content in CN frameworks. Pristine g-C₃N₄ materials derived from common precursors (*e.g.*, melamine, dicyandiamide, urea, and triazole) have triazine frameworks, which frequently suffer from a rapid recombination rate

of photoexcited charge carriers, large bandgaps around 2.7 eV, and low electrical conductivity,[10–12] severely limiting their photocatalytic and electrocatalytic activities.[13,14] To address these issues, developing and tailoring g-C$_3$N$_4$ with novel molecular structures and atomic arrangements from various precursors becomes one straightforward approach. For example, Mane *et al.* synthesised mesoporous *s*-heptazine-based C$_3$N$_5$ by calcinating 3-amino-1,2,4-triazole, and the as-prepared C$_3$N$_5$ presented a narrower bandgap of 2.2 eV, leading to enhanced light absorption and improved photocatalytic H$_2$ production.[15] Shankar and coworkers achieved azo-linked *s*-heptazine-based C$_3$N$_5$ by sintering 2,5,8-trihydrazino-*s*-heptazine with a narrow bandgap of 1.76 eV and electron-rich basicity.[16] In 2018, Kim and colleagues prepared a nanoporous C$_3$N$_5$ from 5-amino-1*H*-tetrazole with combined triazole and triazine moieties, illustrating a decent catalytic performance on hybridising with graphene for the oxygen reduction reaction (ORR).[7] Our group recently utilised aminoguanidine hydrochloride as the precursor to synthesise a tetrazine-based C$_3$N$_{5.4}$ with excellent sensing ability for water molecules.[9] All the results mentioned above indicate the pivotal importance of carbon nitride molecular structures with high nitrogen contents (*i.e.*, C$_3$N$_5$, C$_3$N$_6$, and C$_3$N$_7$) to the performance of particular applications.[7,9,15,17,18]

Incorporating heteroatoms (*e.g.*, B, S, N, and P) into the CN lattice has been demonstrated as a practical way of modifying the electronic and chemical properties of g-CN, which can significantly improve their light absorption, redox potential, carrier mobility, and catalytic activity.[6,19,20] In addition, doping heteroatoms can behave as trapping sites for photoexcited electrons/holes to suppress their recombination.[21–23] As early as 2010, Cheng and coworkers first synthesised S-doped carbon nitride (SCN) by placing bare g-CN in gaseous H$_2$S at high temperatures.[24] The resultant SCN exhibited an increased valence band (VB) width and an elevated conduction band (CB) minimum owing to a homogeneous substitution of lattice N by the doped S content, which showed boosted activities for hydrogen evolution and photooxidation of phenol. As a common precursor, thiourea has been widely used to construct SCN,[25] and it has been well acknowledged that the doped sulfur can either substitute the lattice carbon atoms[26] or nitrogen atoms.[27] In this regard, the replacement of the edge nitrogen atom with sulfur can be more favourable considering the similar electronegativities of N and S.[19] However, all sulfur doping in these studies is still based on the conventional triazine g-CN framework, and the S content is low (less than 0.3 wt%) due to the small ratio of S in precursors and poor thermodynamic stability of S in the g-CN matrix, which remains a crucial challenge prior to commercialization.

Herein, we report on the synthesis of novel SCNs *via* facile self-assembly of 5-amino-1,3,4-thiadiazole-2-thiol (5-ATDT) at various temperatures for the first time. The as-obtained SCNs exhibit new molecular structures composed of a combination of thiadiazole, triazole, and triazine frameworks with a high sulfur content (from 3.59 wt% to 0.35 wt% at 350 °C and 550 °C, respectively). As the carbonation temperature increases, the sulfur sites are gradually substituted by carbon/nitrogen, and

the bandgap decreases accordingly. In addition to sophisticated spectroscopic analyses, theoretical density functional theory (DFT) calculations are conducted to confirm the thermodynamic stability of the proposed chemical structures. The photocatalytic hydrogen evolution reaction (HER) activities of these SCNs are experimentally measured to demonstrate their great potential for practical applications.

The chemical composition of SCN samples is measured by CHNS. The chemical composition of SCN-350, SCN-450, SCN-550, and SCN-575 is C$_3$N$_{5.09}$S$_{0.13}$, C$_3$N$_{4.76}$S$_{0.05}$, C$_3$N$_{4.58}$S$_{0.01}$, and C$_3$N$_{4.57}$S$_{0.003}$, respectively (Table S1†), corresponding to sulfur percentages of 3.59 wt%, 1.53 wt%, 0.35 wt%, and 0.09 wt%. These results confirm the existence of sulfur in SCNs. Interestingly, the S content decreases from 3.59 to 0.09 wt% on increasing the calcination temperature from 350 °C to 575 °C. At the same time, the N percentage remains almost the same, suggesting that sulfur has low thermodynamic stability in the C matrix and is gradually replaced by carbon/nitrogen at an elevated temperature. It should be noted that we fix a carbon stoichiometric number of 3 for easy comparison with conventional g-C$_3$N$_4$, so the decrease in the nitrogen stoichiometric number ought to be ascribed to the increase in the carbon content. This conclusion can be further confirmed by the pungent egg smell from the quartz tube furnace after calcination, possibly caused by the release of H$_2$S. From a practical perspective, it should be mentioned that the product yield of SCN-575 is negligible, with less than 0.08 g of product from 3 grams of precursor, compared to 0.6 g yield for SCN-550 and more than 1 g for SCN-450.

The powder XRD patterns of SCNs prepared at different calcination temperatures are shown in Fig. 1a. All the samples have two pronounced peaks at around 13 and 27°, ascribed to (100) and (002) reflections of the g-CN-like structure. When the synthesis temperature is increased, the (002) diffraction peak gradually shifts from $2\theta = 26.9°$ (350 °C) to 27.3° (550 °C), corresponding to the interlayer distance decreasing from 0.331 to 0.326 nm by using Bragg's equation. The shrunken interlayer distance of the (002) plane should be attributed to the loss of the large radius sulfur atoms in the layered CN architecture, which can also be conducive to interlayer charge transfer. Notably, the intensity of the (002) peak enhances on increasing the calcination temperature from 350 to 550 °C, indicating improved crystallinity at high carbonisation temperatures. As an exception, the intensity of the (002) peak of SCN-575 is lower as compared to that of SCN-550 (Fig. S1†), suggesting a crystalline reduction if the carbonation temperature is close to the vaporisation point of the precursor at ≈600 °C (Fig. S2†), demonstrated by the thermogravimetric analysis (TGA) measurement.

Fig. 1b illustrates the SEM image of SCN-550 solid particles, which shows a wrinkled surface with a pore structure, possibly owing to the H$_2$S release during the carbonation process. Consequently, the specific surface areas increase consistently with increasing calcination temperatures (Fig. 1c), especially for SCN-575, with an almost doubled specific surface area of 19.1 m^2 g^{-1} compared to SCN-550 (Fig. S3†). The layered architecture of SCN-550 can be clearly confirmed by the TEM image (Fig. 1d), and the zoomed-in large-area HRTEM image (Fig. 1e) shows

12838 | *J. Mater. Chem. A*, 2023, **11**, 12837–12845

This journal is © The Royal Society of Chemistry 2023

Fig. 1 (a) Powder XRD patterns of the SCN samples. The enlarged (100) and (002) reflection peaks are shown in (i) and (ii), respectively. (b) SEM of the SCN-550 particle. (c) N_2 adsorption–desorption isotherms of the SCN samples. (d) TEM image and zoomed-in HRTEM image of SCN-550, and the zoomed-in HRTEM image displaying the lattice spacing of the (002) plane in (e). (f) EDS mapping images of SCN-550.

a lattice spacing of around 0.33 nm, which is consistent with the interlayer distance of the (002) plane from the XRD results. The energy dispersive X-ray spectroscopy (EDS, Fig. 1f) mapping further confirms that sulfur is homogeneously dispersed on the particles with a mass percentage of 0.27%, consistent with CHNS analysis.

Fig. 2 Proposed polymerisation reaction route of 5-ATDT. The final schematic SCN structure composed of one thiadiazole-based unit (i) and eight triazole-based units (ii).

This journal is © The Royal Society of Chemistry 2023

J. Mater. Chem. A, 2023, 11, 12837–12845 | 12839

The possible polymerisation reaction route of 5-ATDT is proposed in Fig. 2. Under a N_2 environment, thiourea (CH_4N_2S) and thiocyanic acid (N≡C–SH) are generated *via* thermal decomposition of 5-ATDT and then gradually polymerised into sulfur-containing unit cells composed of one thiadiazole and two triazine moieties (i). Simultaneously, the release of H_2S during the calcination process leads to another triazole-based moiety (ii), whose number quickly boosts as the calcination temperature increases. The final SCNs comprise these two building blocks (i) + (ii), while their number ratios depend on the synthesis temperatures. For example, SCN-450 has a chemical composition of $C_3N_{4.76}S_{0.05}$, roughly equal to the reaction of 1 thiadiazole-based unit (i) and 11 triazole-based units (ii). On the other hand, the sulfur ratio of SCN-550 dramatically dropped and is less than 0.4 wt%, equal to 1 thiadiazole-based unit (i) and 59 triazole-based units (ii).

DFT calculations were carried out in order to confirm the stability of the proposed chemical structures of SCNs. As previously mentioned, SCN-450 is comprised of 1 (i) and 11 (ii), and we mark it as SCN-12 here. For comparison, we have also considered the situation of SCN-9, which should be composed of 1 (i) and 8 (ii). Since SCN-9 has a higher sulfur concentration than SCN-12, its calcination temperature should be lower than 450 °C. The optimised 2D monolayered structures of SCN-9 and SCN-12 are shown in Fig. 3a and b. SCN-9 and SCN-12 structures are constructed considering $3 \times 3 \times 1$ and $4 \times 3 \times 1$ supercells of $C_3N_{4.8}$ (unit (ii)) and $C_3N_{4.2}S_{0.6}$ (unit (i)) to form 116 atoms and 155 atoms of overall stoichiometry as $C_3N_{4.67}S_{0.067}$ and $C_3N_{4.7}S_{0.05}$, respectively. Both SCN-9 and SCN-12 are represented as a monoclinic lattice, with lattice parameters of $a = 16.94$ Å, $b = 20.06$ Å, and $\gamma = 113.2°$ for SCN-9 and $a = 22.59$ Å, $b = 20.06$ Å, and $\gamma = 113.2°$ for SCN-12. The interatomic distances of the structures are provided in Table S2†. For both the structures, average distances of N–N, C–N, S–C, and S–N are

1.40 Å, 1.35 Å, 1.90 Å, and 2.00 Å, respectively. The cohesive energy (E_{coh}) and formation energy (E_F) of the structures are calculated as:

$$E_{coh} = \frac{E_{S-gCN} - (n_C E_C + n_N E_N + n_S E_S)}{n_C + n_N + n_S} \quad (1)$$

$$E_F = \frac{E_{S-gCN} - (n_C \mu_C + n_N \mu_N + n_S \mu_S)}{n_C + n_N + n_S} \quad (2)$$

where E_{S-gCN}, E_C, E_N, E_S are the energies of the SCN-9 (or SCN-12) 2D monolayer, and isolated C, N, and S atoms, respectively. μ_C, μ_N, and μ_S are the chemical potentials of C, N, and S atoms derived from graphite, N_2 gas, and hexagonal S_8 systems, respectively. n_C, n_N, and n_S are the numbers of C, N, and S atoms within the monolayers. Notably, SCN-9 and SCN-12 exhibit a cohesive energy [formation energy] of −7.99 eV per atom [−4.54 eV per atom] and −8.00 eV per atom [−4.57 eV per atom], which is comparable to the cohesive energy of the stable g-$C_3N_{4.8}$ (−8.04 eV per atom [−4.65 eV per atom]) structure as calculated on the present level of theory, indicating that both SCN-9 and SCN-12 are thermodynamically stable. More importantly, the cohesive/formation energies of SCN-12 are smaller than those of SCN-9, indicating enhanced thermal stability of SCNs with less sulfur content (higher calcination temperatures).

The charge density and electron localisation function (ELF) plots are provided in Fig. 3c and d. The ELF is a dimensionless quantity that measures the possibility of finding one electron in the vicinity of another electron in a molecule/atom, thereby revealing the type of bonding. The range of the ELF lies from 0 to 1, in which '1' refers to perfect localisation of electrons, *i.e.*, the most durable covalent bond, '0.5' refers to a metallic bond, and 0 < ELF < 0.5 refers to an ionic bond. Within SCN-9 and SCN-12, higher charge accumulation and more intense electron
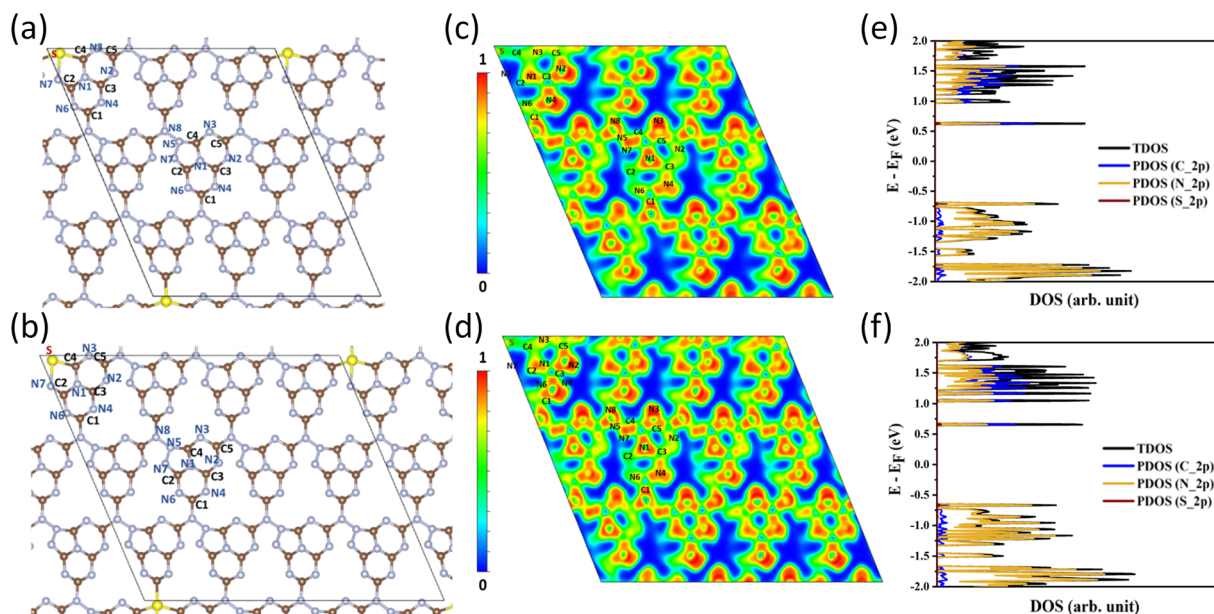

Fig. 3 (a) and (b) Optimised structures of SCN-9 and SCN-12. (c) and (d) 2D ELF plot of SCN-9 and SCN-12. (e) and (f) TDOS and PDOS plots of SCN-9 and SCN-12.

12840 | *J. Mater. Chem. A*, 2023, **11**, 12837–12845

This journal is © The Royal Society of Chemistry 2023

density distribution are found at the C–N bonds compared to at C–S and N–S bonds. This finding infers the covalent nature of C–N bonds but the ionic nature of C–S and N–S bonds, in which the hybrid bonding enables the rich physicochemical properties and multifunctional applications.

For a better understanding of the physiochemical properties of SCNs, the total/partial densities of states (TDOS/PDOS) of SCN-9 and SCN-12 are provided in Fig. 3e and f. The bandgap (direct) values of SCN-9 and SCN-12 are 1.33 eV and 1.31 eV, respectively. The underestimated bandgap values are attributed to the consideration of the GGA-PBE functional instead of a more accurate but computationally expensive hybrid functional (*e.g.*, Heyd–Scuseria–Ernzerhof). However, the trend of the bandgap evolution is in good correspondence with the experimental findings, which will be discussed later. As evident from the PDOS plots, the VB of both SCN-9 and SCN-12 are contributed by the N-2p, whereas C-2p and N-2p PDOS both contribute to the CBs.

In order to confirm our proposed structure of SCNs, the chemical bond states were systematically studied *via* spectroscopic characterization studies. The Fourier-transform infrared (FT-IR) spectra of SCNs are first investigated (Fig. S4†). All the samples present multiple peaks in the range of 1242–1637 cm^{-1}, owing to the typical stretching modes of C–N heterocycles.[28] The band at 810 cm^{-1} is a characteristic of tri-*s*-triazine,[7] and the broadband at 3000–3600 cm^{-1} corresponds to N–H stretching vibration mode due to the terminal amino group or

adsorbed water molecules.[9,29] Remarkably, the band at 2163 cm^{-1} should be assigned to C≡N band stretching vibration modes, but this peak intensity gradually decreases for samples calcined at higher temperatures, possibly because of the reaction of decomposed N≡C–SH under the high-temperature treatment. Furthermore, near-edge X-ray absorption fine structure (NEXAFS) and X-ray photoelectron spectroscopy (XPS) are utilised to examine the chemical bonds of SCNs. In the C K-edge NEXAFS spectra (Fig. 4a), three main characteristic resonances are presented at 285.2 eV, 288.0 eV, and 293.6 eV.[30] The first peak centred at 285.2 eV should be assigned to π^*_{CaC}, and the last peak at 293.6 eV should correspond to π^*_{CaN}.[31,32] Notably, the peak at 288.0 eV is ascribed to sp^2-hybridized carbon with nitrogen heterocycles (π^*_{N-CaN}), and a blue shift can be observed when the calcination is at higher than 350 °C, indicating an enhanced N–C≡N bond strength upon the formation of a triazine moiety at higher temperatures. N K-edge NEXAFS spectra of SCNs show three distinct peaks at 399.4 eV, 401.3 eV, and 402.3 eV (Fig. 4b). The first peak at 399.4 eV should be attributed to aromatic N atoms with two neighbouring C atoms in the heptazine hetero-ring (π^*_{N-CaN}). The peaks at 401.3 eV and 402.3 eV should be linked with the graphitic three-fold central nitrogen atoms in heptazine (π^*_{N-3C}) and sp^3 N–3C bridging among the three structural heptazine units (π^*_{N-3C}), respectively.[31,33] Likewise, the increased peak intensity at 402.3 eV hints at the gradual connection between individual heptazine units. In the S K-edge NEXAFS spectra (Fig. 4c), a sharp

Fig. 4 (a) C K-edge, (b) N K-edge, and (c) S K-edge XANES spectra of the SCN samples. (d) High-resolution XPS C 1s, (e) N 1s spectra, and (f) S 2p of the SCN samples.

This journal is © The Royal Society of Chemistry 2023

J. Mater. Chem. A, 2023, **11**, 12837–12845 | **12841**

peak at ≈2472 eV in all the SCN samples suggests the presence of heterocyclic sulfur in the structure.[8,34]

The XPS spectra of SCNs are also exploited to identify their surface chemical compositions and confirm the proposed structure. As shown in Fig. S5,† the XPS survey spectra of SCNs confirm the existence of N, O, and C elements, with a weak but visible S 2p peak for SCN-350 and SCN-450. The S 2p signal is almost undetectable for samples calcined at 500 °C and 550 °C, demonstrating the severe sulfur loss at high temperatures. As shown in Fig. 4d–4f, C 1s XPS peaks are able to be deconvoluted into two main components: one sharp peak at ≈288 eV ought to be assigned to the sp^2 C atoms bonded with the neighbouring N atoms in heptazine (N–C=N), and one lower peak at 284.6 eV corresponds to the sp^2-hybridized carbon bonds (C–C=C) owing to N defects in the carbon nitride structure.[17,35] N 1s XPS curves mainly exhibit two distinct peaks at 398.9 eV and 400 eV and one broad peak at 404.5 eV with relatively low intensity, corresponding to N–C=N, N–C3, and N–N bonds, respectively.[9,36] Most importantly, the S 2p curves of SCNs are shown in Fig. 4f, and the peak intensity dramatically decreases when temperatures increase from 350 °C to 550 °C. The peak at 164.0 eV is attributed to the C–S–C bonds in the aromatic ring, and the peak at 165.2 eV is ascribed to thiazolium-like S–C–N bonds. The peaks at 168.0 eV and 169.2 eV suggested the existence of S–O bonds, possibly from the surface-adsorbed oxygen or other oxygen-containing functional groups.

The beneficial effect of S incorporation into carbon nitrides and the novel molecular structure is further experimentally demonstrated by optical characterization studies, which can directly reflect their optical bandgap and carrier lifetime, thereby determining solar light conversion efficiency. UV/vis spectra of SCNs demonstrate an intrinsic semiconductor-like absorption behaviour, as shown in Fig. 5a. Interestingly, the optical bandgaps gradually decrease on increasing the sintering temperatures from 350 °C (2.68 eV) to 550 °C (2.44 eV) (Fig. S6a†), which is consistent with the previous DFT calculations. The steady-state PL characteristics of SCNs excited with 370 nm light were studied using fluorescence spectroscopy, as displayed in Fig. S6b.† The photoemission peaks for SCNs were gradually redshifted from 453 nm (2.73 eV) for SCN-350 to 495 nm (2.50 eV) for SCN-550, which exhibit a consistent tendency with slightly larger values compared with the results from UV-vis spectroscopy, presumably caused by indirect recombination of photogenerated carriers. As the calcination temperatures increase, the PL intensity increases accordingly, revealing an improved crystallinity. To confirm the band position, the Mott–Schottky plots of SCNs are measured, as shown in Fig. S6c,† in which the CB position moved to a negative direction from −0.95 V (vs. Ag/AgCl at pH 7) for SCN-350 to −1.05 V, −1.12 V and −1.24 V for SCN-450, SCN-500, and SCN-550, respectively. Accordingly, their valence band positions were derived from the CB position and optical bandgaps (Fig. S6d†); the CB values of SCNs are below the reduction potential of protons, revealing that photoinduced electrons in the CB reach the thermodynamic requirement to reduce H^+ to hydrogen under light illumination. The CB position of SCN-550 is more negative than the
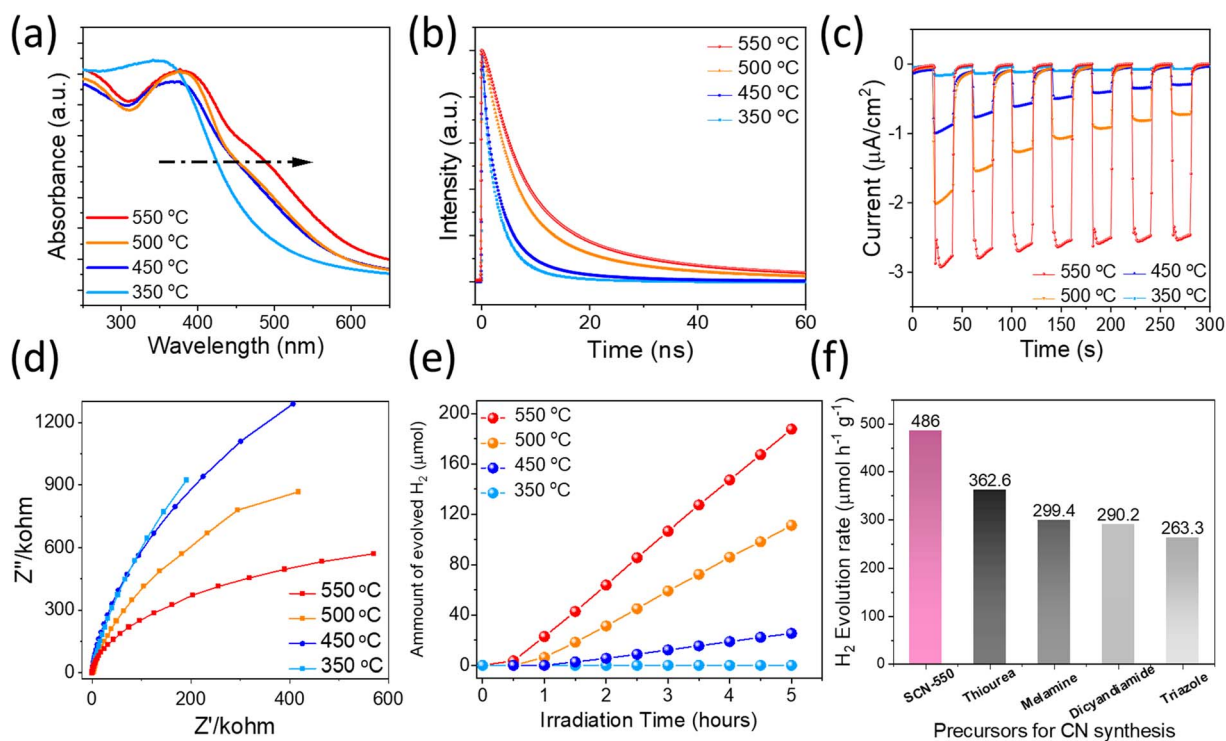

Fig. 5 (a) UV-vis diffuse reflectance, (b) TRPL spectra, (c) transient photocurrent responses, and (d) EIS Nyquist plots of the SCN samples. (e) Photocatalytic H_2 evolution with a 1.5 G air-mass filter for the SCN samples. (f) Photocatalytic H_2 evolution rates of SCN-550 and bulk g-CN derived from common precursors (including ATDA, thiourea, melamine, dicyandiamide, and triazole) with the same calcined conditions (550 °C per 3 hours).

12842 | J. Mater. Chem. A, 2023, 11, 12837–12845

This journal is © The Royal Society of Chemistry 2023

others, thus enabling a higher capability to reduce protons and produce H_2.

To further verify the crystalline quality and effect of trap density, carrier dynamics of SCNs were investigated by using time-resolved PL (TRPL) spectra, as depicted in Fig. 5b. The extracted carrier lifetimes, τ_1 and τ_2 related to non-radiative recombination and intrinsic radiative recombination, are given in Table S3† using a biexponential decay function fitting. SCN-550 exhibited the longest PL lifetime of 11.6 ns, demonstrating that an improved crystallinity hinders the annihilation of charge carriers. These values are longer than those of g-C_3N_4 derived from common precursors, such as melamine,[37] urea,[38] and dicyandiamide.[39] Therefore, more electrons are expected to participate in the photocatalytic HER, possibly leading to the excellent performance of SCN-550. In addition, the bandgap of SCN-550 is considerably lower than that of g-C_3N_4 with a typical bandgap of 2.7 eV,[25] exhibiting great potential in photocatalytic water splitting applications. Photocurrent measurements are exploited to probe the carriers' separation efficiency at the photocatalysts/electrolyte interface, so the transient photocurrent response of the SCNs was measured. The samples were subjected to seven cycles of intermittent illumination with solar light. Fig. 5c depicts the transient photocurrent as a function of time without any bias potential. For SCN-350, no obvious photocurrent was observed, while the photocurrents rapidly increased when the light was turned on for other samples and then returned to their original level after turning off the light. This transient photocurrent was able to be switched ON/OFF repeatedly for multiple cycles. Notably, the photocurrent of SCN-550 was considerably higher than that of the others without any decay during the cycling measurement, and no obvious photocurrent decay occurred during the illumination process either, indicating better crystallinity, enhanced charge-carrier transport with fewer electron–hole recombination, and a broader light absorption range. We further conducted electrochemical impedance spectroscopy (EIS) analysis to reveal the separation of charge carriers and interfacial transfer efficiency in SCNs, providing direct evidence of carrier charge separation and the contribution to H_2 evolution. Generally, a smaller arc radius in the EIS curves hints at the higher transfer efficiency of interfacial charges. Fig. 5d shows EIS Nyquist plots of all SCN photoelectrodes without an external bias, in which the arc radius of SCN-550 is smaller, again suggesting that the interfacial charge transfer resistances gradually decrease with increasing calcination temperatures, resulting in improved charge separation and transport.

Because SCNs have special band structures with small bandgap energy, we studied their photocatalytic HER activities in deionised water using a Newport Class ABB solar simulator with a 1.5 G air-mass filter. In the experiment, 3 wt% of platinum (Pt) was loaded on SCNs as a co-catalyst by *in situ* photo-deposition, and 10 vol% triethanolamine (TEOA) was used as a hole scavenger.[40,41] As depicted in Fig. S7,† the photoinduced electrons at the CB of SCNs are transported to Pt sites and react with protons, leading to hydrogen evolution. Simultaneously, the photoexcited holes are scavenged by oxidising TEOA into [(2-hydroxy-ethyl-(2-oxo-ethyl)-amino)]acetaldehyde or [bis-(2-hydroxy-ethyl)-amino]acetaldehyde.[42] In the beginning, the HER rate is relatively low because of the slow photo-reduction process, which converts the co-catalyst from Pt^{2+} to Pt on the surface of SCNs. Afterwards, the activity gradually increases after activating active sites by continuous illumination, and all the samples can sustainably generate H_2 with decent hydrogen production rates (Fig. 5e and Table S4†), which increase steadily with a prolonged light irradiation duration. On increasing the carbonation temperatures, the hydrogen evolution rate increases accordingly, and SCN-550 exhibits the highest production rate with 188 µmol H_2 after five hours of illumination (*ca.* 486 µmol h^{-1} g^{-1}), 60% higher than that of pristine g-C_3N_4 derived from a series of typical g-CN precursors calcined under the same condition (Fig. 5f).[42] The enhanced photoactivity should be attributed to the smaller bandgaps (Fig. S8†) and improved charge carrier transfer rate, which significantly enhances the absorption in the solar spectrum's visible regime and contributes to overcoming the water-splitting reaction's thermodynamic barrier. The solar-to-hydrogen energy conversion efficiency (STH) of SCN-550 was calculated by using the following equation STH (%) = $\dfrac{r \times \Delta G \times 100}{P \times S}$, where r, ΔG, P and S are the hydrogen evolution rate (0.048 mmol h^{-1}), the Gibbs free energy change of the water splitting reaction (237 kJ mol^{-1}), the power of irradiated solar light (1 sun = 0.1 J s^{-1} cm^{-2}) and the area of light irradiation (54 cm^2), respectively. The STH value for SCN-550 was evaluated to be 0.06%. Fig. S9† shows the long-term stability measurement for SCN-550 over four cycles, suggesting no obvious decrease in the HER rate.

In summary, we have demonstrated the first design and synthesis of thiadiazole-based sulfur-doped carbon nitrides using 5-ATDT. Systematic DFT calculations and spectroscopic studies reveal that thiadiazole-derived sulfur-doped CNs are stabilised with the structure consisting of triazole and triazine moieties with small ratios of thiadiazole on the edge, in which the sulfur sites attach to the edge of the structure and are gradually substituted by carbon as the calcination temperature is increased. Compared with the pristine carbon nitrides derived from common precursors, the resultant SCNs possess a significantly narrowed bandgap, an extended visible light absorption regime, and optimal electronic properties for the photocatalytic HER. Among the materials prepared, SCN-550 exhibits an H_2-generation rate of 486 µmol g^{-1} h^{-1}, which is about 60% higher than that of g-CN derived from conventional precursors. We believe that these novel sulfur-doped carbon nitrides open the opportunity to design a new family of nanomaterials with enhanced properties for photocatalysis, batteries, solar cells, and sensing applications.

Author contributions

AV conceived the idea and supervised the project. XG directed the project and synthesised SCN samples. XG, MF and ZL carried out photocatalytic HER measurements. RS conducted DFT band structure calculations under the supervision of SC. C–HL, ZL, and LH carried out CHNS, XPS, TRPL, and microscopy characterisation under the supervision of TW. NPD and MF

This journal is © The Royal Society of Chemistry 2023

J. Mater. Chem. A, 2023, **11**, 12837–12845 | **12843**

conducted the electrochemical measurements with the help of J-HY. XZ, PK and JY provided constructive opinions and suggestions. XG drafted the manuscript. All the authors discussed and contributed to the results.

Conflicts of interest

There are no conflicts to declare.

Acknowledgements

References

1 F. K. Kessler, Y. Zheng, D. Schwarz, C. Merschjann, W. Schnick, X. C. Wang and M. J. Bojdys, *Nat. Rev. Mater.*, 2017, **2**, 1.

2 L. H. Lin, Z. Y. Lin, J. Zhang, X. Cai, W. Lin, Z. Y. Yu and X. C. Wang, *Nat. Catal.*, 2020, **3**, 649.

3 D. M. Zhao, Y. Q. Wang, C. L. Dong, Y. C. Huang, J. Chen, F. Xue, S. H. Shen and L. J. Guo, *Nat. Energy*, 2021, **6**, 388.

4 X. Guan, Z. Li, X. Geng, Z. Lei, A. Karakoti, T. Wu, P. Kumar, J. Yi and A. Vinu, *Small*, 2023, e2207181.

5 S. N. Talapaneni, G. Singh, I. Y. Kim, K. AlBahily, A. H. Al-Muhtaseb, A. S. Karakoti, E. Tavakkoli and A. Vinu, *Adv. Mater.*, 2020, **32**, e1904635.

6 H. Wang, Y. R. Bian, J. T. Hu and L. M. Dai, *Appl. Catal., B*, 2018, **238**, 592.

7 I. Y. Kim, S. Kim, X. Jin, S. Premkumar, G. Chandra, N. S. Lee, G. P. Mane, S. J. Hwang, S. Umapathy and A. Vinu, *Angew. Chem., Int. Ed.*, 2018, **57**, 17135.

8 W. Cha, I. Y. Kim, J. M. Lee, S. Kim, K. Ramadass, K. Gopalakrishnan, S. Premkumar, S. Umapathy and A. Vinu, *ACS Appl. Mater. Interfaces*, 2019, **11**, 27192.

9 C. I. Sathish, S. Premkumar, X. Z. Chu, X. J. Yu, M. B. H. Breese, M. Al-Abri, A. H. Al-Muhtaseb, A. Karakoti, J. B. Yi and A. Vinu, *Angew. Chem., Int. Ed.*, 2021, **60**, 21242.

10 W. J. Ong, L. L. Tan, Y. H. Ng, S. T. Yong and S. P. Chai, *Chem. Rev.*, 2016, **116**, 7159.

11 L. C. Chen and J. B. Song, *Adv. Funct. Mater.*, 2017, **27**, 1702695.

12 Y. Hou, A. B. Laursen, J. Zhang, G. Zhang, Y. Zhu, X. Wang, S. Dahl and I. Chorkendorff, *Angew. Chem., Int. Ed.*, 2013, **52**, 3621.

13 J. Liu, H. Wang and M. Antonietti, *Chem. Soc. Rev.*, 2016, **45**, 2308.

14 X. Wang, A. Vasileff, Y. Jiao, Y. Zheng and S. Z. Qiao, *Adv. Mater.*, 2019, **31**, e1803625.

15 G. P. Mane, S. N. Talapaneni, K. S. Lakhi, H. Ilbeygi, U. Ravon, K. Al-Bahily, T. Mori, D. H. Park and A. Vinu, *Angew. Chem., Int. Ed.*, 2017, **56**, 8481.

16 P. Kumar, E. Vahidzadeh, U. K. Thakur, P. Kar, K. M. Alam, A. Goswami, N. Mahdi, K. Cui, G. M. Bernard, V. K. Michaelis and K. Shankar, *J. Am. Chem. Soc.*, 2019, **141**, 5415.

17 S. N. Talapaneni, G. P. Mane, D.-H. Park, K. S. Lakhi, K. Ramadass, S. Joseph, W. M. Skinner, U. Ravon, K. Al-Bahily and A. Vinu, *J. Mater. Chem. A*, 2017, **5**, 18183.

18 I. Y. Kim, S. Kim, S. Premkumar, J. H. Yang, S. Umapathy and A. Vinu, *Small*, 2020, **16**, e1903572.

19 L. B. Jiang, X. Z. Yuan, Y. Pan, J. Liang, G. M. Zeng, Z. B. Wu and H. Wang, *Appl. Catal., B*, 2017, **217**, 388.

20 H. S. Gujral, G. Singh, A. V. Baskar, X. Guan, X. Geng, A. V. Kotkondawar, S. Rayalu, P. Kumar, A. Karakoti and A. Vinu, *Sci. Technol. Adv. Mater.*, 2022, **23**, 76.

21 M. Z. Rahman and C. B. Mullins, *Acc. Chem. Res.*, 2019, **52**, 248.

22 L. Hu, X. W. Guan, T. Wan, C. H. Lin, S. Q. Liu, R. B. Zhu, W. J. Chen, Y. Yao, C. Y. Huang, L. Yuan, S. Shahrokhi, D. W. Chu, C. Cazorla, J. F. Chen, J. Yang, S. B. Yi, S. J. Huang and T. Wu, *ACS Energy Lett.*, 2022, **7**, 4150.

23 C. Y. Huang, H. Li, Y. Wu, C. H. Lin, X. Guan, L. Hu, J. Kim, X. Zhu, H. Zeng and T. Wu, *Nano-Micro Lett.*, 2022, **15**, 16.

24 G. Liu, P. Niu, C. Sun, S. C. Smith, Z. Chen, G. Q. Lu and H. M. Cheng, *J. Am. Chem. Soc.*, 2010, **132**, 11642.

25 K. Wang, Q. Li, B. S. Liu, B. Cheng, W. K. Ho and J. G. Yu, *Appl. Catal., B*, 2015, **176**, 44.

26 J. D. Hong, X. Y. Xia, Y. S. Wang and R. Xu, *J. Mater. Chem.*, 2012, **22**, 15006.

27 C. H. Lu, P. Zhang, S. J. Jiang, X. Wu, S. Q. Song, M. S. Zhu, Z. Z. Lou, Z. Li, F. Liu, Y. H. Liu, Y. Wang and Z. G. Le, *Appl. Catal., B*, 2017, **200**, 378.

28 L. Shi, K. Chang, H. B. Zhang, X. Hai, L. Q. Yang, T. Wang and J. H. Ye, *Small*, 2016, **12**, 4431.

29 L. Ye, Q. H. Liang, Z. H. Huang, Y. Lei, C. Z. Zhan, Y. Bai, H. Li, F. Y. Kang and Q. H. Yang, *J. Mater. Chem. A*, 2015, **3**, 18860.

30 K. G. Latham, W. M. Dose, J. A. Allen and S. W. Donne, *Carbon*, 2018, **128**, 179.

31 Y. Zheng, Y. Jiao, Y. Zhu, L. H. Li, Y. Han, Y. Chen, A. Du, M. Jaroniec and S. Z. Qiao, *Nat. Commun.*, 2014, **5**, 3783.

32 H. Yabuta, M. Uesugi, H. Naraoka, M. Ito, A. L. D. Kilcoyne, S. A. Sandford, F. Kitajima, H. Mita, Y. Takano, T. Yada, Y. Karouji, Y. Ishibashi, T. Okada and M. Abe, *Earth, Planets Space*, 2014, **66**, 1.

33 K. G. Latham, M. I. Simone, W. M. Dose, J. A. Allen and S. W. Donne, *Carbon*, 2017, **114**, 566.

34 A. M. El-Sawy, I. M. Mosa, D. Su, C. J. Guild, S. Khalid, R. Joesten, J. F. Rusling and S. L. Suib, *Adv. Energy Mater.*, 2016, **6**, 1501966.

35 K. Akaike, K. Aoyama, S. Dekubo, A. Onishi and K. Kanai, *Chem. Mater.*, 2018, **30**, 2341.

36 J. W. Fang, H. Q. Fan, M. M. Li and C. B. Long, *J. Mater. Chem. A*, 2015, **3**, 13819.

12844 | *J. Mater. Chem. A*, 2023, **11**, 12837–12845

This journal is © The Royal Society of Chemistry 2023

37 S. Nayak, L. Mohapatra and K. Parida, *J. Mater. Chem. A*, 2015, **3**, 18622.

38 J. Fu, K. Liu, K. Jiang, H. Li, P. An, W. Li, N. Zhang, H. Li, X. Xu, H. Zhou, D. Tang, X. Wang, X. Qiu and M. Liu, *Adv. Sci.*, 2019, **6**, 1900796.

39 G. Dong, Y. Wen, H. Fan, C. Wang, Z. Cheng, M. Zhang, J. Ma and S. Zhang, *RSC Adv.*, 2020, **10**, 18632.

40 X. Wang, K. Maeda, X. Chen, K. Takanabe, K. Domen, Y. Hou, X. Fu and M. Antonietti, *J. Am. Chem. Soc.*, 2009, **131**, 1680.

41 J. M. Lee, J.-H. Yang, N. H. Kwon, Y. K. Jo, J.-H. Choy and S.-J. Hwang, *Dalton Trans.*, 2018, **47**, 2949.

42 J. H. Yang, S. Kim, I. Y. Kim, J. M. Lee, J. B. Yi, A. Karakoti, S. Joseph, K. Albahily and A. Vinu, *Sustainable Mater. Technol.*, 2020, **25**, e00184.